Am J Physiol Heart Circ Physiol 298: H1249–H1259, 2010.
First published January 15, 2010; doi:10.1152/ajpheart.00363.2009.

Comparative structural and hemodynamic analysis of vascular trees

J. Yang,[1] L. X. Yu,[1] M. Y. Rennie,[1,2] J. G. Sled,[1,2] and R. M. Henkelman[1,2]

[1]*Mouse Imaging Centre, The Hospital for Sick Children, Toronto;* [2]*Department of Medical Biophysics, University of Toronto, Toronto, Ontario, Canada*

Submitted 13 April 2009; accepted in final form 15 January 2010

Yang J, Yu LX, Rennie MY, Sled JG, Henkelman RM. Comparative structural and hemodynamic analysis of vascular trees. *Am J Physiol Heart Circ Physiol* 298: H1249–H1259, 2010. First published January 15, 2010; doi:10.1152/ajpheart.00363.2009.—The availability of detailed three-dimensional images of vascular trees from mammalian organs provides a wealth of essential data for understanding the processes and mechanisms of vascular patterning. Using this detailed geometric data requires the ability to compare individual representations of vascular trees in statistically meaningful ways. This article provides some comparisons of geometry and also of simulated hemodynamics, enabling the identification of similarities and differences among 10 individual specimens (5 placenta specimens and 5 lung specimens). Similar comparisons made with a series of models (starting with the simplest and increasing in complexity) enable the identification of essential features that are needed to account for the patterns and function of vascular arborization.

microcomputed tomography; vessel morphology; hemodynamics; lung; placenta

THE DEVELOPMENT of vascular networks is critical for biological functions. The vasculature is required for the delivery of oxygen and nutrients to tissues and for the removal of waste products. To accomplish this, the arborization of the vasculature has developed to distribute blood throughout the tissue so that all cells are, on average, within 100 μm of a small vessel (2). This proximity allows for efficient exchange processes. In the lung, the vascular tree provides a large surface area at the alveoli to allow for gas exchange. In the placenta, the fetal vasculature has evolved to present an extensive area for exchange with the maternal vascular system. In all of these functions, the vascular arborization appears in some way to be optimized for efficiency of function either delivering blood with minimum work or using minimum materials for the distribution system (19).

The development of the vasculature must be prescribed in the genome. However, beyond the major vessels, which are patterned under tight genetic control, the fine branching is more stochastic and appears to arise from recursive patterning rules (17). It is quite clear that the vascular arborization is not prescribed by a "blueprint." The apparent self-similar structure or fractal pattern suggests that the genome provides rules for branching that are applied repeatedly (8, 13).

It is also clear that vascular patterning can be severely disrupted by genetic changes and by diseases (10). Changes in genes that are known to be essential for vascular patterning, such as VEGF and Tie2, cause highly abnormal patterns of vascular arborization (5, 11). Disease states, such as cancer, present with abnormal vascular patterns including corkscrew vessels, trifurcations, and atrioventricular shunts (15).

If we want to distinguish abnormal or aberrant vascularization, we need to have ways of comparing individual vascular trees. To do this, we need to be able, given two actual biological vascular trees, to address the following question: "Are these two vascular trees effectively the same or are they different?" To make this comparison in a more than descriptive and qualitative manner requires the development of statistical methods for summarizing vascular trees that are meaningful from a biological and physiological perspective. It is the purpose of this report to define some of these statistical summaries.

The question about the equivalence of vascular trees is becoming much more poignant given developments in three-dimensional (3-D) imaging that are providing fully 3-D images of actual biological vascular trees. These 3-D images can be obtained in vivo using angiography with injected contrast and X-ray imaging (12) or with flow-sensitized MRI (14). At a more detailed level, 3-D vascular images can be obtained in vitro with microcomputerized tomography (micro-CT) after the injection of a radioopaque contrast agent (3) or with optical projection tomography (or optical CT) using fluorescently labeled vascular endothelium (28). These 3-D images are rich in detail and can be extracted by computer to provide extensive morphological data for the comparison of actual trees. The explosion in 3-D vascular images is just beginning and cries out for meaningful statistical methods of comparison. It is also likely that further improvements in 3-D imaging and additional developments in computer representations will make these data more complete and more valuable in the coming years.

We recognize that the quantitative and comparative analysis of vascular trees is required to address a number of different questions in vascular biology and pathophysiology:

First, given genetically identical and normal individuals (inbred mice) raised in controlled and disease-free environments, what is the range of variation of statistical abstractions of these presumably equivalent vascular trees from a particular organ (7)? Can we determine the "consistant features" of this group of equivalent vascular trees? How can these features be related to genes and genetic pathways that are known to be involved in the control of vascular arborization?

Second, if we consider a different group of vascular arborizations (a different organ, a different inbred strain, or a different diet) but still a normal and genetically identical set of vascular trees, are these additional trees distinguishable from the group in the first question? Do they show the same features or do they differ in some statistical sense?

Third, if we analyze a group of abnormal vascular trees [deliberate mutations, mouse models of human disease such as hereditary hemorrhagic telangiectasia (1), or chronic physiological stress such as high blood pressure (18)] in what statis-

Address for reprint requests and other correspondence: R. M. Henkelman, Mouse Imaging Centre, The Hospital for Sick Children, Toronto Centre for Phenogenomics, 25 Orde St., Toronto, Ontario, Canada M5T 3H7 (e-mail: mhenkel@phenogenomics.ca).

tically measurable and physiologically meaningful ways are these trees different? Do these differences arise from the genetic rule set that builds the original tree or do they result from secondary remodeling?

Finally, with the growing interest in theoretical models of the process of vascular arborization as a way of understanding the biological systems, when can we conclude that a model is equivalent to a group of actual biological vascular trees? Can we use a hierarchy of such model building to parse the essential features of vascular arborization?

This set of questions represents a far-reaching and long-range agenda for the study of vascular arborization. This report takes some initial steps at determining measures of statistical abstraction that we believe are robust, are based on group averages of equivalent vascular trees, and are physiologically motivated. However, the abstractions we identify certainly represent only an initial list and will eventually need to be expanded. We used measures that we have developed to specifically analyze five fetoplacental arterial trees and five pulmonary arterial trees from an inbred strain of mice, looking for similarities and differences between the two types of trees. The two organs were chosen for comparison due to their simple bifurcating trees and primary functions as exchange organs. We then compared the results of these experimental abstractions with a hierarchy of increasingly more complicated theoretical models, beginning with a simple symmetrical bifurcating self-similar tree governed by Murray's law (19) and then making the models more sophisticated to identify some of the essential features needed to account for the biologically measured vascular arborizations. We show that with a relatively simple model based on both anatomic form and physiological function that we are able to match many of the features of the placental tree but that a more complicated two component model is required to account for some of the structure evident in the lung vasculature.

MATERIALS AND METHODS

All experimental protocols were approved by and carried out in accordance with the guidelines set forth by the Animal Care Committee of the Hospital for Sick Children.

A more detailed description of the experimental methods is provided in the Supplemental Material but consisted of the following steps:[1]

Step 1. Fetoplacental and lung samples (5 each) were prepared by perfusing the arterial vascular tree, which had been filled with a solid radioopaque contrast agent (Microfil, Flow Tech).

Step 2. 3-D X-ray micro-CT images were acquired and reconstructed with volume elements numbering 50–75 million over each organ. Illustrative CT images of one placenta and one lung are shown in Fig. 1.

Step 3. Vessel segments and bifurcations were identified automatically by computer and represented as a connected graph of skeletonized centerlines and straight pipes of diameters equal to the computed mean diameters between adjacent bifurcations.

Step 4. Hemodynamic flow was calculated through this network of pipes assuming a realistic but representative pressure drop, a laminar flow pattern, and a correction for blood viscosity at small diameters (22). From these flow calculations, pressure and wall shear throughout the whole tree were calculated for each specimen.

[1] Supplemental Material for this article is available online at the *American Journal of Physiology-Heart and Circulatory Physiology* website.

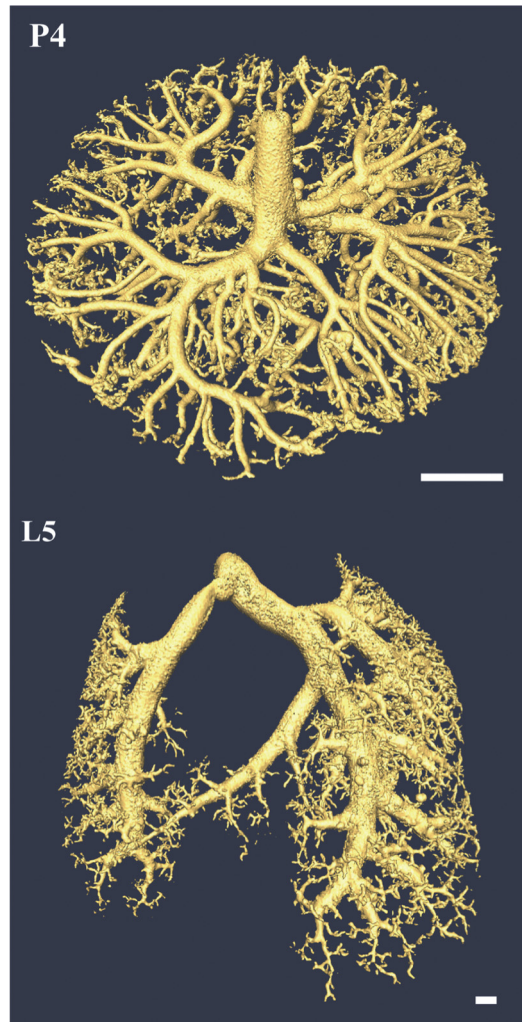

Fig. 1. Isointensity surface rendering of microcomputed tomography (micro-CT) images of *placenta sample 4* (P4) and *lung sample 5* (L5). Scale bars = 1 mm.

Step 5. Finally, a hierarchal set of five increasingly complex theoretical models of vascular tree structure and flow were developed using geometric parameters extracted from the measured micro-CT images (Table 1) until they accounted for the major features of the biological vascular tree.

RESULTS

Figure 2 shows pressure distributions calculated over the five placental and five lung vascular trees. The placental trees showed strong similarity in shape to each other, although there was not a simple mapping of the bifurcation structure throughout the five biological examples. In contrast to the placentas, the lung vascular trees showed a quite different overall shape, representative of the shape and structure of lungs. In particular, the vasculature could be qualitatively divided into feeder vessels, which take blood to each of the lobes of the lung, and then a distribution arborization, which provides blood to the individual alveoli. The feeder vessels represent a fairly reproducible anatomic pattern in which homologous bifurcations out to several orders could be recognized on all five samples. However, the smaller vessels were more stochastic in their patterning. The pressure distributions were qualitatively similar across

Table 1. *Parameter design for hierarchy models*

	Model Feature Included					Estimated Parameters	
	Model I	*Model II*	*Model III*	*Model IV*	*Model V*	Placenta	Lung
Murray's law exponent = 3.0	Yes					3.0	3.0
Diameter of input artery, mm	Yes	Yes	Yes	Yes	Yes	0.38 ± 0.02	0.74 ± 0.12
Two lung ranges, mm	Yes	Yes	Yes	Yes	Yes		$d < 0.116$ and $d > 0.116$
Segment length-to-diameter ratio	Yes	Yes	Yes	Yes	Yes	3.1 ± 0.2	2.3 ± 0.1 and 2.6 ± 0.2
Experimental branching exponent		Yes	Yes	Yes	Yes	3.5 ± 0.2	6.0 ± 0.5 and 2.8 ± 0.1
Branching asymmetry coefficient			Yes	Yes	Yes	0.15 ± 0.02	0.11 ± 0.01 and 0.14 ± 0.02
Fractional variance of length-to-diameter ratio				Yes	Yes	2.6 ± 0.2	1.4 ± 0.04 and 1.6 ± 0.2
Microcomputed tomography resolution cutoff and variance, %					Yes	0.044 ± 10	0.066 ± 10

Values are means ± SE. The parameters used for the models were estimated from vasculatures of placentas and lungs. "Yes" represents parameters used for individual models; *d*, diameter.

each of the five illustrative examples. In all cases, the pressure went from high pressure in the inflow vessel to zero pressure at the outflow vessels. The pressure drop was estimated from the literature and was nominally set to 1.0 mmHg for the placenta and 21 mmHg for the lung. The intermediate pressures tended to correspond similarly to the level of vessel generation from sample to sample. Because pressure is a continuous variable throughout the tree (unlike flow or segment number, which are discontinuous across bifurcations), it can serve admirably as an ordering principle for subsequent statistical analysis.

Figure 3, *top*, shows the associated flow patterns for one fetoplacental vasculature (P4) and one representative lung (L5). The flow is shown on a logarithmic plot with flow values ranging over six orders of magnitude for the placental example and eight orders of magnitude over the lung. The mean ± SD of the simulated flow in the placentas was 2.7 ± 0.5 mm^3/s, whereas the mean ± SD of the simulated flow in the lungs was considerably higher at 210 ± 99 mm^3/s. Figure 3, *bottom*, shows calculated wall shear stress, which was constrained to within a factor of threefold in values over both the lung and placenta, confirming that uniform wall shear is one of the target objectives of vascular remodeling.

Figures 2 and 3 show patterns of arborization and distributions of flow, pressure, and shear over the vasculatures of the placenta and lung in which qualitative differences between the organs can be appreciated visually. However, it is not yet possible to quantitatively interpret similarities and differences between such complex arborized structures. To assist in this

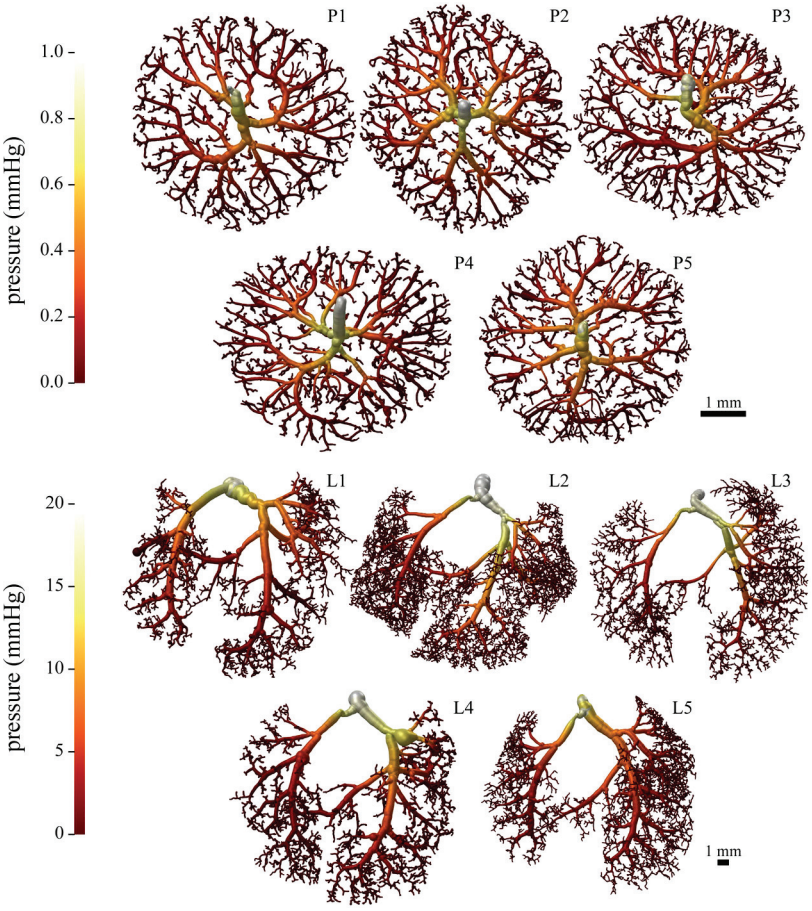

Fig. 2. Pressure distributions over vascular trees of 5 placentas (P1–P5) and 5 lungs (L1–L5). The inlet and outlet pressures for placenta were scaled to 1.0 and 0 mmHg, whereas the inlet and outlet pressures for lungs were scaled to 21 and 0 mmHg. Scale bars = 1 mm.

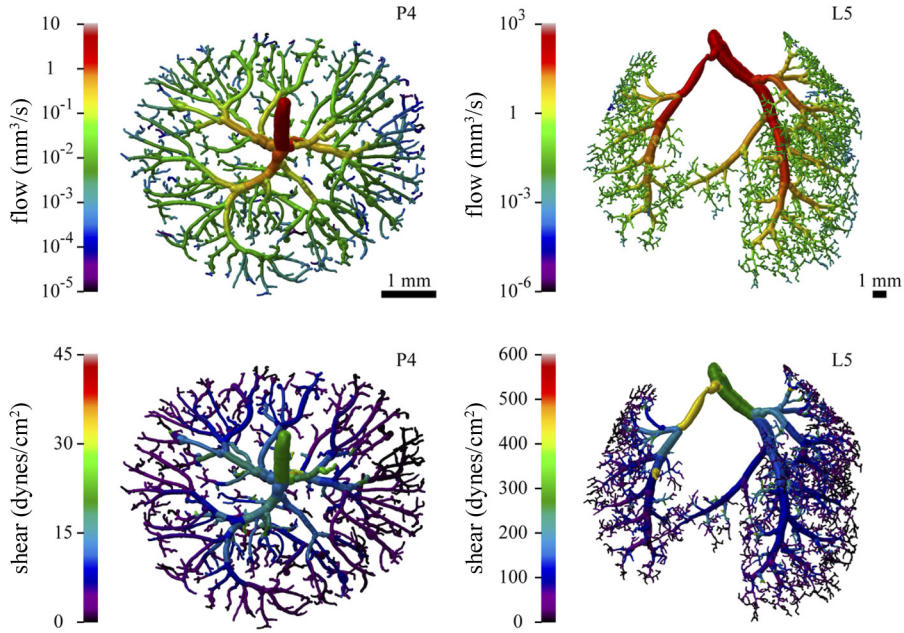

Fig. 3. Flow (log scale) and shear distributions over vascular trees of P4 and L5. Scale bars = 1 mm.

interpretation, we developed statistical summaries and compared these with interpretative models.

Figure 4 shows cumulative distributions of number of vessels with a diameter larger than the ordinate diameter. Such cumulative distributions are useful for several reasons: *1*) they allow for easy comparisons between individual vascular trees, *2*) they give a direct indication of whether or not the vascular tree is fractal, and *3*) they provide a direct readout of the number of vascular segments that are identified in these micro-CT images. For the fetoplacental samples, this corre-

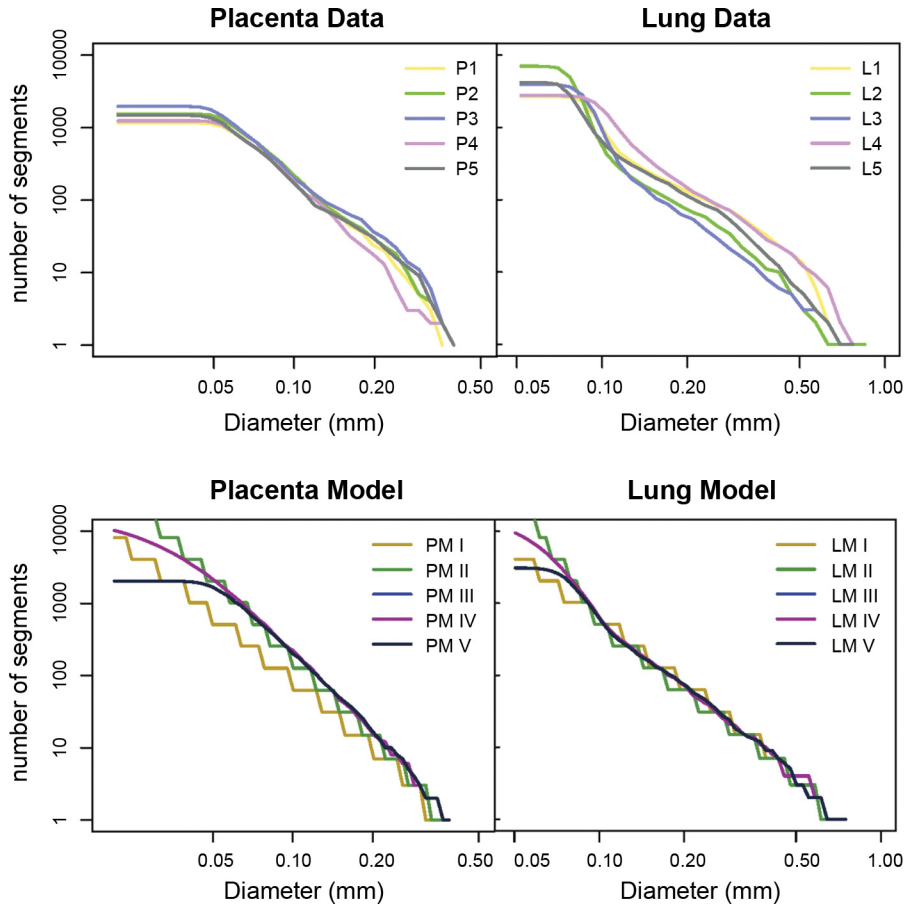

Fig. 4. Cumulative distribution of the number of segments with diameter *d* greater than the ordinate value. Cumulative distributions plots have the advantage that they are independent of bin sizes and that they provide a direct visualization of the total number of vessel segments detected in the tree. Data are plotted on a log-log scale for the placentas and lungs with experimental values shown at the *top* and model calculations shown at the *bottom*. There are 35–40 data points for each curve that are uniformly distributed on the log diameter scale with each step corresponding to an increase of 1.075. The lines are straight line segments connecting the data points. Representations of the data points have been omitted for clarity. It should be noted that in the model calculations, the results for *model III* and *model IV* are exactly superimposed and are represented by the line for *model IV*. PM I–PM V, *models I–V* for the placenta; LM I–LM V, *models I–V* for the lung.

sponded to 1,470 ± 300 vessels, and for the lung samples, it corresponded to 4,120 ± 1,770. These cumulative distributions were remarkably similar for samples within each of the two organs studied. The placental data were approximately a straight line on this log-log plot until it leveled out at diameters smaller than ~0.05 mm in diameter. The heterogeneity at the large vessel end corresponded to the asymmetry factors of the first few bifurcations. This heterogeneity quickly merged into a consistent pattern of vessels by ~0.15 mm in diameter, corresponding to 6.5 generations.

The lung data shown in Fig. 4 also showed general similarity between the five samples. In this organ, the number of vessels with a size of greater than diameter d was not a straight line on a log-log plot but had a change in slope at ~0.12 mm in diameter for all of the lung vascular trees. Again, there was a leveling out of the distributions when the resolution of the micro-CT was no longer able to make vessel images that were segmentable by the computer algorithm.

Figure 5 shows the joint distributions of flow and diameter for all segments from each specimen. For all examples, the general trend was that smaller segments have smaller flow but at any particular diameter there was considerable heterogeneity over the flow in segments of the same size. Nevertheless, there was remarkable similarity in the joint distributions of flow and diameter. As a final summary, the average distribution for the placenta and lung showed the average of the data over the five individual samples. In comparing the lung with placental data, it can be seen that the lung has a large input vessel with a larger flow and that the smallest limited vessel diameter detected is larger than that of the placenta and reflects the poorer spatial resolution achieved in the lung CT images.

Figure 6 shows model flow and diameter distributions of placenta and lung which are discussed later.

Figure 7, *top*, shows the calculation of shear that was shown qualitatively in Fig. 3, *bottom*. In Fig. 7, the average of the median shears calculated for each of the measured vascular trees is plotted as a function of pressure throughout the tree. The choice of pressure rather than diameter for the ordinate has the advantage that pressure is a continuous variable throughout the tree including at the bifurcations. The dotted lines in Fig. 7 delimit a band containing 67% of the shear measures over all individual vessel segments at a particular pressure. This is a measure of shear heterogeneity from vessel segment to vessel segment. The green error bars in Fig. 7 represent the SD of the median shear as a function of pressure over the five samples in each anatomic structure. These error bars are considerably less than the SD over vessel segments and demonstrated that although the individual segments at a given pressure showed significant variation in shear, on average the shears in the complete vascular tree systems were remarkably similar. Finally, the observation from these data is that shear ranges only over a factor of fivefold for the placenta and lung even though the flow rates range over six and eight orders of magnitude for the placenta and lung, respectively. This confirms the well-known observation that vascular remodeling is adapting vessel diameters in a way that minimizes the variation of shear over the whole tree (19). However, it has also been shown that additional functional controls are needed to account for remodeling (20, 21).

In the results discussed so far, we have shown several statistical summaries of fetoplacental and lung vascular trees. Clearly, there could be other paired correlations and even higher dimensional correlations that could be considered, but we believe that what we have shown is representative. We have shown that although the particular details of the vascular tree within either of these organs can differ considerably, the overall system properties of the geometry of the tree and the flow through it are remarkably consistent within samples from the same organ. We have also shown at several points that there are qualitative and significant differences between placental vascular trees and lung vascular trees. However, these similarities and differences remain descriptive at this point. In the next section, we attempt to understand the features of these statistical summarizes in terms of a hierarchical set of theoretical models.

Calcuation of vascular properties for a hierachical set of models. In an attempt to understand the features of the data shown in Figs. 4, 5, and 7, we calculated the expected values from very simple through to more complex theoretical models to ascertain which features are essential in such models to account for the statistical summaries of the measured data. This cascade of model complexity is shown in Table 1, and the models are represented by *models 1–5* (MI–MV). The simplest model of which one can conceive for a self-similar vascular tree is a symmetric bifurcation of daughter vessels at each generation with the daughter vessels following Murray's law (19). Murray's law makes the assumption that the diameter of a parent vessel (d_0) is related to the diameters of the two daughter vessels (d_1 and d_2, respectively) according to the following power-law relationship given by *Eq. 1*:

$$d_0^k = d_1^k + d_2^k \quad (1)$$

Murray claimed that if the exponent k was equal to 3 then the vascular tree would have optimal properties in the sense that it would require minimum energy to distribute blood to the smallest generation daughter vessels or, alternatively, that the construction of the tree would require minimal wall material to build. Such a tree has idealized properties that are self-similar over scale. Such a simple model tree has only a discrete set of vessel diameters, as shown in Fig. 4, *bottom*, for the placenta and lung (yellow curves). On this logarithmic plot of cumulative number of segments versus diameter, the Murray's law model with $k = 3$ exhibits a stepped function with a slope of −3 for both the placenta and lung. In all the model calculations presented in this report, the models are followed for a total of 14 generations, which provides greater detail than is needed for the subsequent analysis while keeping computer time reasonable. This simplest model represents the generalized multiscale character of both the placenta and lung vascular trees but fails to account for much of the specific structure. In Fig. 6, we can see this lowest-level model (MI) in terms of the predicted flow versus diameter distribution. In this different representation, this simple model again has only discrete data points that correspond to the 14 generations of the model and for which the slope of the flow versus diameter is given by 3 on a log-log plot (29). Again, while this model captures the general multiscale nature of the actual vascular trees, it is too simplistic to model the features of the measured distributions.

For the simplistic Murray's law (MI), shear can be seen to be constant for all high pressures in both organs but decreasing toward the terminal arterioles except for a slight increase for

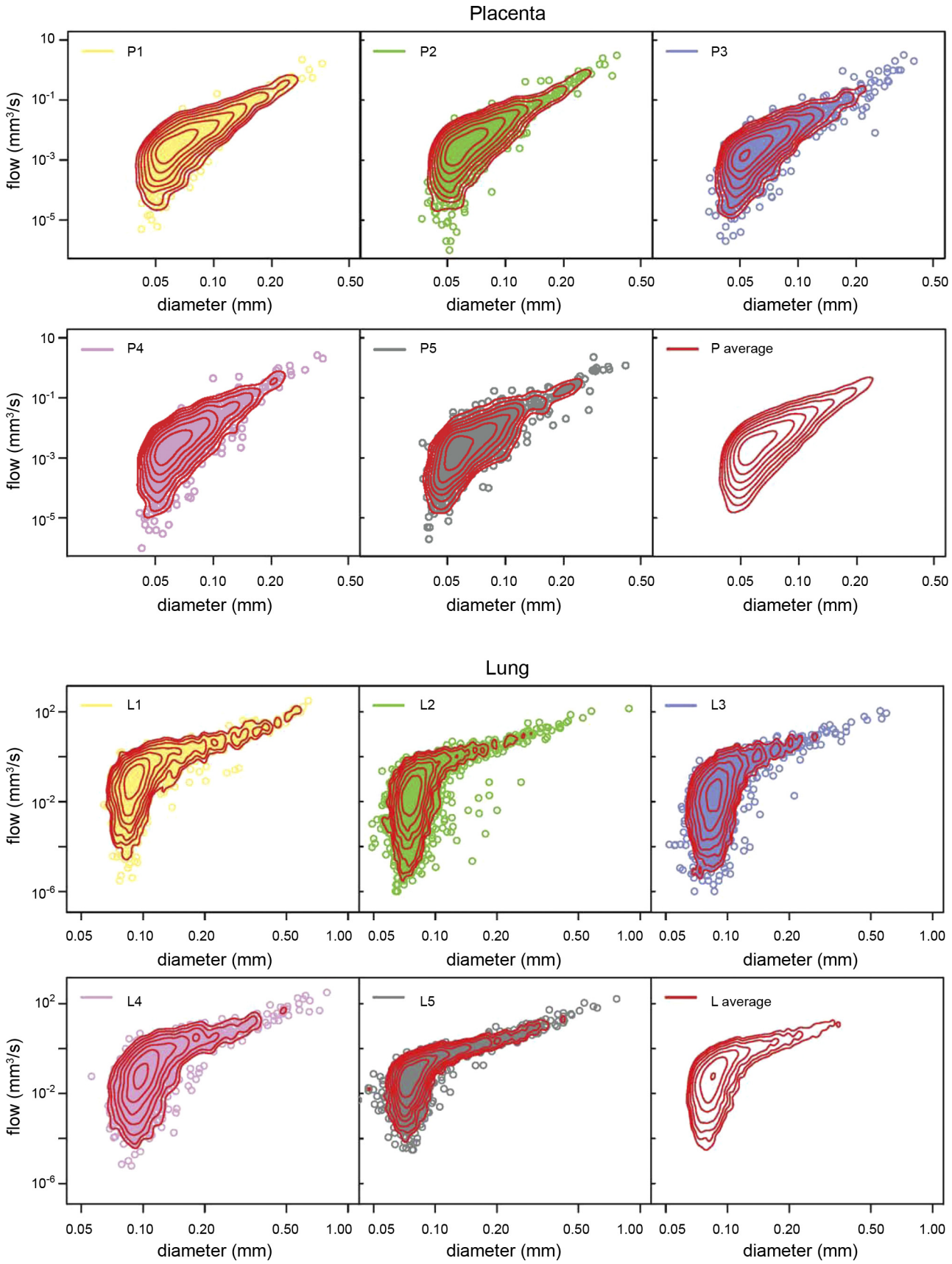

Fig. 5. Joint distributions of flow and diameter for placentas and lungs on a log-log scale. There is a single circular point for each vessel segment, but since they coalesce due to the large number of segments, the distributions are also represented by seven evenly space contours overlaid in red. The "average" distributions resulted from all the segments in each of the five samples, renormalized by five.

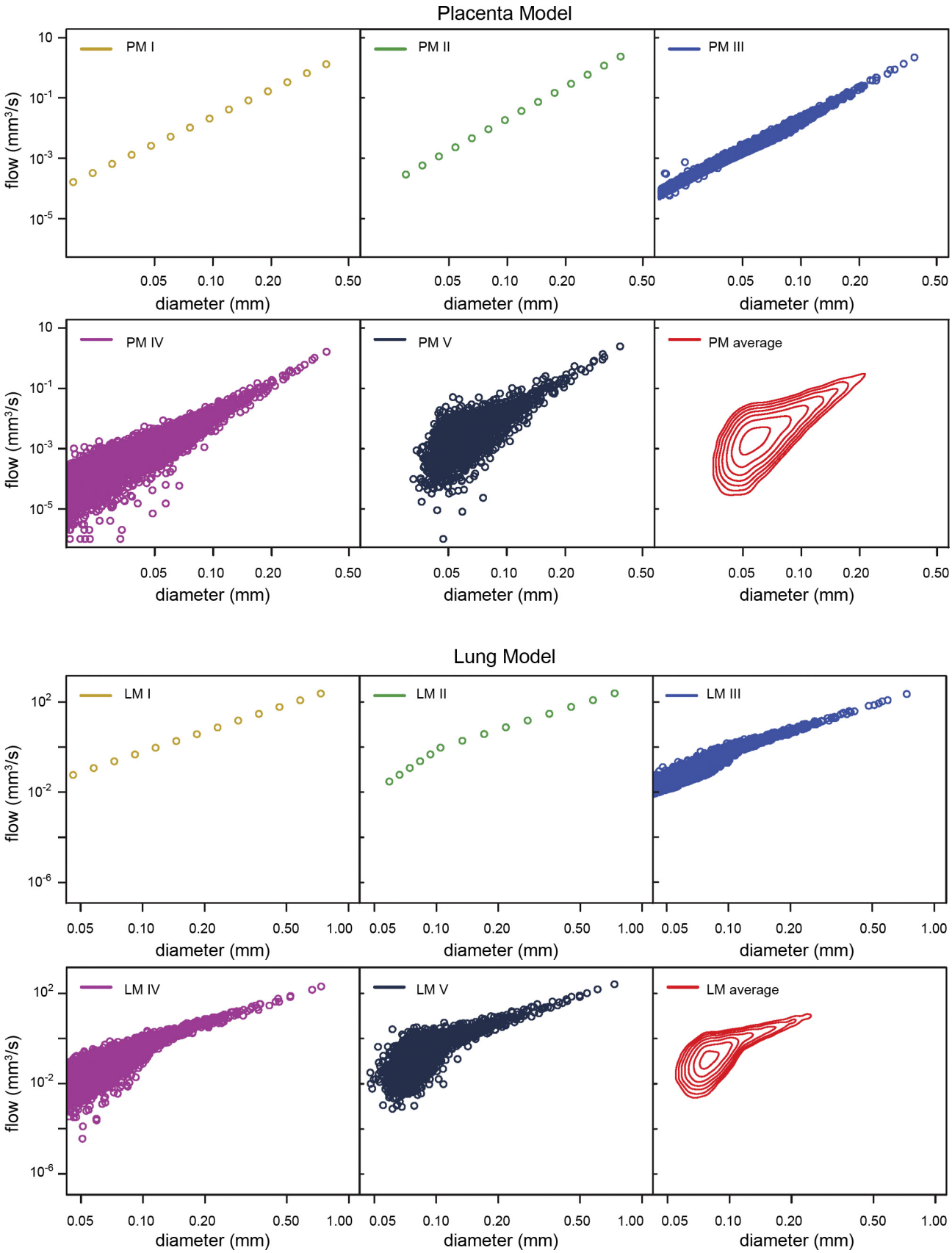

Fig. 6. Flow and diameter distributions of placenta and lung models on a log-log scale. The red curves represent contours over five independent cases for *model V* of the placenta and lung respectively.

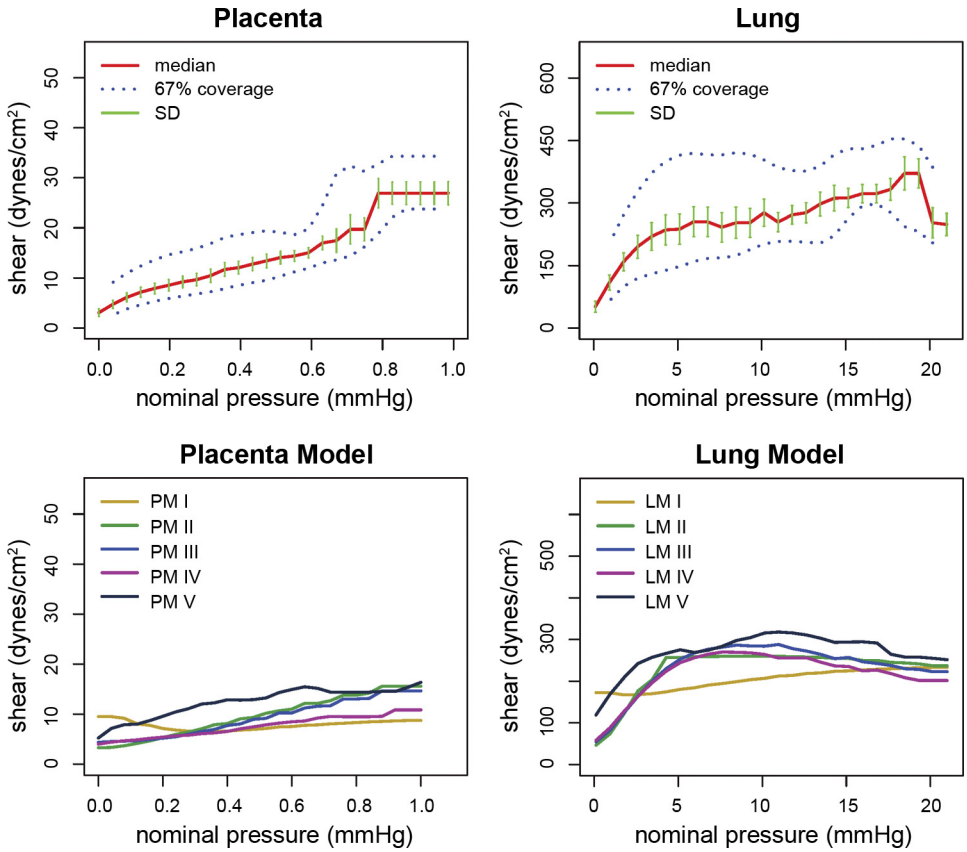

Fig. 7. Relationship between shear and relative pressure. The *top* graphs correspond to the statistics of *samples 1–5*. The red lines represent mean shear stress, the dotted blue lines present 67% coverage of shear stress away from the mean, and the green error bars are SDs of median shear stress over the five samples. The *bottom* graphs correspond to *models I–V*. Data are binned in 26 uniformly spaced pressures from 0 to maximum pressure.

the smallest vessels (Fig. 7, *bottom*). This decrease is due to the effective decrease in viscosity at small diameters (22). If the viscosity was kept constant, shear would also have been constant, as has been previously reported using Murray's model (data not shown).

A somewhat more sophisticated model results from allowing the exponent in the Murray's model to take on values derived from the experimentally measured data. This is represented by *model II* (MII). The exponent for the model is extracted from measurements of the diameter ratios of the parent and two daughters at each bifurcation over all the branch points in the five samples of each organ. From these measures, an experimental value of k can be generated for each bifurcation. The median k for the placental data is 3.5 ± 0.2 (Table 1). For the lung data, as has been pointed out by others (4, 27), there is no single exponent that accounts for the full range of vascular diameters. Thus, the exponent of the bifurcation was extracted from large vessels (diameter > 0.116 mm) to be 2.8 ± 0.1 and for the vessels <0.116 mm to be 6.0 ± 0.5. This cutoff was chosen as the average of the intersections of fitted lines to the straight sections in Fig. 4, *top right*.

The effect of using experimental values of k is shown in Figs. 4, 6, and 7. For the placental model (PMII), the cumulative plot of a number of segments versus diameter now has a steeper slope of -3.5, which is a better approximation to the experimental data shown in Fig. 4. In terms of flow and diameter joint distributions (Fig. 6), the slope of PMII is steeper and corresponds to a slope of space 3.5. Also, the range of the diameters is diminished with this higher value of k such that the smallest vessels at *generation 14* are ~0.03 mm in diameter. In terms of the model shear shown in Fig. 7, shear is no longer constant but is larger for the largest vessels and diminishes in the smaller vessels.

For the lung data, LMII introduces several additional factors, but these are easy to understand in terms of the model changes. First of all, the diminished value of k to 2.8 for vessels >0.116 mm in diameter results in a lower slope in the cumulative distribution plot (Fig. 4, LMII) than had been seen with the simple Murray's model. However, the change in slope to a higher value below 0.116 mm results in a steeper slope in the cumulative distribution model, which ultimately surpasses the simple Murray's model at diameters <0.08 mm. This same behavior can be seen in Fig. 6 in the flow versus diameter models, where LMII shows a lower slope from the root vessel down to 0.116 mm and then a steeper slope beyond this point. The model shear in Fig. 7 behaves as would be anticipated with an increasing shear from the root vessel down to 0.116 mm and then a significantly decreasing shear thereafter, leaving a maximum in the shear distribution curve around a pressure of 2 mmHg. In all cases, the choice of a bifurcation exponent derived from measured values brings the model into closer agreement with experimental measurements. In addition, the division of the lung vascular tree into two separate ranges begins to develop a structure that more closely resembles the bilinear shape of the number of segments versus diameter in the experimental lung data. However, this model still has only discrete possible diameters and does not allow for enough variation to account realistically for the measured flow patterns in particular.

A more realistic model can allow for asymmetric daughters at every branching point (24). This additional variation is added in *model III* (MIII) where the variance in the asymmetrical branching ratio is measured from the experimental data and values are shown in Table 1. The most obvious effect of this increase in model complexity is that the simulated data are no longer discrete, resulting in a continuous distribution of diameters. [It should be noted that the results of MIII are coincident with those of *model IV* (MIV).] This can clearly be seen in Fig. 4, *bottom*, in which MIII maintains much of the shape and slope of MII but fills in the step function with a continuous spread of diameters. This can also be seen in Fig. 6, in which the flow versus diameter now becomes a continuous band tracking the discrete data points in MII and also generating many more small-diameter vessels below the limit of vessels in MII. This is because as branches become asymmetric, the smaller diameter branches continue to bifurcate into even smaller branches in a cumulative nature. This cumulative bias toward smaller branches also accounts for the curvature at low diameters seen in both the placental and lung models of MIII in Fig. 4. This asymmetrical branching makes the model more realistic but still fails to account for the variability in the flow at a particular diameter size as seen in Fig. 6 compared with the measured data in Fig. 5. That is, the flow versus diameter distributions for MIII remains within a tight band with a little additional scatter at the low end due to the small diameter correction for blood viscosity.

At the next level of complexity we allow, at any particular diameter, for variation in the length of the vessel segment. Up to this point in the calculation, the length has been strictly proportional to the diameter, with the ratios given by the experimentally derived mean length to diameter ratio β (as shown in Table 1). Now, the variation in length for a given diameter is extracted from all the segments in the measured micro-CT data trees. The measured variation is described as σ^2_{LD} in Table 1. The effect of this variation in length can be seen most clearly in Fig. 6, where MIV shows considerably more heterogeneity in the flow at each vessel diameter for the placental and lung model. This modification certainly brings the model data much more in line with the measured distributions for the five placenta and five lungs. This addition of variable length has no effect on the cumulative distributions shown in Fig. 4 since the number of segments of each diameter remains the same. Thus, the curves for MIII and MIV remain superimposed in Fig. 4.

The final adjustment to the models does not change the fundamental nature of the model but adapts the model data to those measured with a micro-CT system of limited resolution. The modeling up to level MIV allows for extremely small vessels limited only by the 14 generations that were calculated. However, vessels smaller than a certain size cannot be detected by the micro-CT system and, therefore, are not included in the simulated experimental data. This can be appreciated in the cumulative number of segments versus diameter graphs in Fig. 4, *top*, where experimentally these graphs plateau to the left of a finite diameter. This "loss of detectability" is modeled as a random process in which the probability of detection as a function of diameter is given by an error function with a half-value set to twice the effective resolution of the micro-CT (16). The slope of the error function is governed by a variance, which was set somewhat arbitrarily to 10% of the cutoff value. These additional model parameters are shown in Table 1 and are *model V* (MV). This detectability threshold effectively prunes small vessels from the model trees, which can be seen in the cumulative distributions as a plateauing of the number of segments at diameters less than the cutoff value. This can also be seen even more dramatically in Fig. 6 in the removal of small-diameter vessels from the flow versus diameter distributions. This pruning of small vessels also has a qualitative effect on the modeled flow versus diameter. When a vessel is removed from the modeled distribution, because it is deemed not to have been detected by the micro-CT system, this changes in subtle ways the complete pattern of flow. Thus, the particular segment with a diameter and flow as shown in Fig. 4 is not just deleted but the whole flow distribution must be recalculated. This yields the results shown in Fig. 6 (MV results), in which the small vessels are no longer detected but the flow distribution is broadened for the smallest remaining vessels. This is a fundamental limitation from the use of a micro-CT system, which is not able to detect vessels down to the capillary level. It also becomes a fundamental limitation on the measured flow distributions in the vascular micro-CT images. Thus, to make the data comparable between the micro-CT biological data and the model simulations, this effect needs to be taken into account.

Overall, MV takes into account sufficient features that provide simulated data that very closely correspond to the measured data for both the placenta and lung. In Fig. 4, the cumulative distributions for the placenta generated by MV would be indistinguishable from the cluster of experimental measurements represented by P1 to P5. The same conclusion can be reached for the lung model (LMV), which lies nicely intermediate within the range of data represented by experiment measures L1 to L5. In terms of the flow distributions, the final frame, consisting of red contours in Fig. 6 for both the placenta and lung, is very similar to that obtained experimentally in the final frames in Fig. 5. There are some minor variations in that there appears to be a slight hump on the top left of the placental model distribution compared with the experimental average. This is not accounted for at this level of modeling, and no explanation is provided. Additionally, the distribution for the lung model has less low flow in small vessels than was measured in the experimental average shown in Fig. 5. Again, the cause for this flow discrepancy has not been established at this time. It may arise from some marginally detected terminal vessels in the micro-CT data having erratic walls, which lead to more restricted simulated flows.

In Fig. 7, the distributions of wall shear versus pressure exhibit minor changes due to the deletion of small vessels but maintain the basic shapes described previously and are reasonably consistent with the experimentally derived shear measurements. Most importantly, the range of shear over the whole trees remains within a factor of two for the MV calculations.

DISCUSSION

In this article, we have shown methods of finding similarities among features of vascular trees from two organs in genetically identical mice. We have proposed some statistical summaries to allow comparisons between individual representations of these vascular trees as a way of identifying similarities. The choice of measures that we used are by no means unique or

complete. One can tabulate multidimensional scatterplots of parent and daughter diameters, segment lengths, and branching angles at every bifurcation in a tree (30). This seems to provide a very complete geometric statistical summary, but when we have plotted some of these, the scatter is broad and the discrimination between same and different is frequently obscured. The challenge, therefore, is to find summary measures that are closely clustered for identical vascular trees and markedly different when the trees are not the same. We have also made use of estimated physiological properties that correspond to the geometric forms of equivalent trees. These interpret the static idealized trees in terms of flow, pressure, and wall shear. Even though the calculation methods for determining these parameters are quite approximate, we believe that the physiological parameters may be a more meaningful context in which to compare vascular trees in that they are more closely related to the function of such trees. Using both the measures of geometry and functional parameters, we have shown that five measured vascular trees from each of the placenta and lung show very close similarity to each other. We have also shown in our simulated models that if we account for variance of all of the measured parameters, we can generate a distribution of trees that essentially overlaps that which we have measured (data not shown). Thus, we believe we have provided a partial set of reasonable metrics for identifying sets of vascular trees that are equivalent.

We have also shown that vascular trees from different organs, even in genetically identical mice, can be recognized as different. The lung vascular trees require a more sophisticated analysis than the placenta to account for the features that have been identified experimentally. In our initial attempts, we tried to model the lung as a single self-similar structure at all scales but were unable to obtain meaningful fits to the measured data and, therefore, opted for dividing the vascular arborization into two different regimens, which much more appropriately accounted for the measurements (26). Although the fundamental differences between the placenta and lung can be recognized in the analysis that we have presented, we have provided no strict objective criteria for determining whether two groups of trees can be regarded as equivalent or whether they must be deemed to have separate features. However, at a qualitative level, we have been able to recognize significant differences between the placenta and lung using the metrics that have been proposed.

Finally, we have also shown how to use the metrics that we have proposed to compare the measured vascular trees with model simulations. Furthermore, we have shown how to add increasing complexity to the models to provide the features that are essential to account for the measured data. We believe that it is this kind of formal comparison between models and measurements of multiple actual trees that will be essential for determining the adequacy with which models account for the features of vascular arborizations. In all of our work, we have used fairly standard and simple imaging and computer analysis and flow simulation. Improvements in all of these could add to greater accuracy and precision in the kind of analysis that we have shown. In particular, CT imaging with a resolution that enabled the complete identification of vessels down to capillary size would give a much more comprehensive picture of the vascular tree and, hence, more accurate flow calculations, including even the venous vasculature. Complete flow calculations over both the arterial and venous systems would circumvent the assumption that has been made in this work: that the smallest detectable arterials all have constant outlet pressure. At the present time, this would require synchrotron light source-based micro-CT (9) to provide sufficient spatial resolution. While advances in this technology have been impressive, specimen coverage over whole organs has not yet attained. The ability to extract vessels by computer analysis would also be improved with increased contrast in micro-CT images. The Microfil contrast agent that we and most other people use has not been optimized to provide maximum intensities for X-ray CT. Better formulations with higher attenuation would allow for smaller vessel detection with a higher level of reliability.

To assess the impact of the micro-CT limit on the minimum detectability of vessels and the effect of the assumption of constant pressure at these terminal vessels, we dissected out one of the lobes of the lung and rescanned it at a nominally $\times 2$ higher resolution (the same as the placentas) and directly compared it with a digitally dissected lobe from the original data. More small vessels were identifiable, and the cumulative distribution extended to smaller diameters and larger numbers. However, within the overlapping range and in the flow, pressure, and shear analysis, the results of the two different resolutions agreed to within the width of the lines on the plots. This result provides reassurance that the analysis that we have done is not critically dependent on the limiting resolution of the micro-CT.

Postprocessing techniques for extracting arborized vessel structures from microCT information also represent an active area of image postprocessing (23). Algorithms that yielded vessel identification at diameters less than the imaging voxel would considerably enhance our methods. Better methods of identifying vascular continuity and for bridging over discrete discontinuities in the micro-CT images would also improve the analysis. More accuracy in the flow calculation, in particular, taking into account the exact nature of the bifurcations (25) and being realistic about flow pulsatility and vessel wall elasticity, would be helpful. Finally, for the comparison of models with measured vascular structures, the identification of quantitative statistical metrics that could determine the adequacy of the feature set of the models to account for the measurements would place this kind of analysis on a firmer analytical basis. Finally, the addition of experimental verification of the calculated flow patterns would increase confidence in the validity of this analysis (6). It is anticipated over the next years that improvements in all of these areas will be forthcoming, enabling much more precise determination of the equivalence of normal and abnormal vascular systems.

In conclusion, we have shown statistical summaries of both geometric and physiological properties of vascular trees derived from direct measurements of real-world biological samples taken from two different organs. We have shown, for the first time, how to use such statistics to distinguish the vasculatures of the two organs, taking into account the variance with each group. Furthermore, we have shown how to use such comparative analysis to determine the adequacy of theoretical models of vascular arborization to account for the biological measurements.

GRANTS

The Mouse Imaging Centre acknowledges funding from the Canada Foundation for Innovation and the Ontario Innovation Trust for providing facilities along with The Hospital for Sick Children. Operating funds from the Ontario Research Development Challenge Fund-Ontario Consortium for Small Animal Imaging and Heart and Stroke Foundation of Ontario Grant T6297 are gratefully acknowledged. R. M. Henkelman holds a Canada Research Chair in Imaging.

DISCLOSURES

No conflicts of interest are declared by the author(s).

REFERENCES

1. **Abdalla SA, Letarte M.** Hereditary haemorrhagic telangiectasia: current views on genetics and mechanisms of disease. *J Med Genet* 43: 97–110, 2006.
2. **Beard DA, Bassingthwaighte JB.** Modeling advection and diffusion of oxygen in complex vascular networks. *Ann Biomed Eng* 29: 298–310, 2001.
3. **Bentley MD, Ortiz MC, Ritman EL, Romero JC.** The use of microcomputed tomography to study microvasculature in small rodents. *Am J Physiol Regul Integr Comp Physiol* 282: R1267–R1279, 2002.
4. **Burrowes KS, Hunter PJ, Tawhai MH.** Anatomically based finite element models of the human pulmonary arterial and venous trees including supernumerary vessels. *J Appl Physiol* 99: 731–738, 2005.
5. **Djonov VG, Galli AB, Burri PH.** Intussusceptive arborization contributes to vascular tree formation in the chick chorio-allantoic membrane. *Anat Embryol (Berl)* 202: 347–357, 2000.
6. **Feintuch A, Ruengsakulrach P, Lin A, Zhang J, Zhou YQ, Bishop J, Davidson L, Courtman D, Foster FS, Steinman DA, Henkelman RM, Ethier CR.** Hemodynamics in the mouse aortic arch as assessed by MRI, ultrasound, and numerical modeling. *Am J Physiol Heart Circ Physiol* 292: H884–H892, 2007.
7. **Glenny R, Bernard S, Neradilek B, Polissar N.** Quantifying the genetic influence on mammalian vascular tree structure. *Proc Natl Acad Sci USA* 104: 6858–6863, 2007.
8. **Glenny RW, Robertson HT.** Fractal properties of pulmonary blood flow: characterization of spatial heterogeneity. *J Appl Physiol* 69: 532–545, 1990.
9. **Heinzer S, Krucker T, Stampanoni M, Abela R, Meyer EP, Schuler A, Schneider P, Muller R.** Hierarchical microimaging for multiscale analysis of large vascular networks. *Neuroimage* 32: 626–636, 2006.
10. **Jin SW, Herzog W, Santoro MM, Mitchell TS, Frantsve J, Jungblut B, Beis D, Scott IC, D'Amico LA, Ober EA, Verkade H, Field HA, Chi NC, Wehman AM, Baier H, Stainier DY.** A transgene-assisted genetic screen identifies essential regulators of vascular development in vertebrate embryos. *Dev Biol* 307: 29–42, 2007.
11. **Jones N, Iljin K, Dumont DJ, Alitalo K.** Tie receptors: new modulators of angiogenic and lymphangiogenic responses. *Nat Rev Mol Cell Biol* 2: 257–267, 2001.
12. **Kidoguchi K, Tamaki M, Mizobe T, Koyama J, Kondoh T, Kohmura E, Sakurai T, Yokono K, Umetani K.** In vivo X-ray angiography in the mouse brain using synchrotron radiation. *Stroke* 37: 1856–1861, 2006.
13. **Krenz GS, Linehan JH, Dawson CA.** A fractal continuum model of the pulmonary arterial tree. *J Appl Physiol* 72: 2225–2237, 1992.
14. **Kruger G, Kleinschmidt A, Frahm J.** Dynamic MRI sensitized to cerebral blood oxygenation and flow during sustained activation of human visual cortex. *Magn Reson Med* 35: 797–800, 1996.
15. **Less JR, Skalak TC, Sevick EM, Jain RK.** Microvascular architecture in a mammary carcinoma: branching patterns and vessel dimensions. *Cancer Res* 51: 265–273, 1991.
16. **Marxen M, Thornton MM, Chiarot CB, Klement G, Koprivnikar J, Sled JG, Henkelman RM.** MicroCT scanner performance and considerations for vascular specimen imaging. *Med Phys* 31: 305–313, 2004.
17. **Metzger RJ, Krasnow MA.** Genetic control of branching morphogenesis. *Science* 284: 1635–1639, 1999.
18. **Molthen RC, Karau KL, Dawson CA.** Quantitative models of the rat pulmonary arterial tree morphometry applied to hypoxia-induced arterial remodeling. *J Appl Physiol* 97: 2354 and 2372–2384, 2004.
19. **Murray CD.** The physiological principle of minimum work. I. The vascular system and the cost of blood volume. *Proc Natl Acad Sci USA* 12: 207–214, 1926.
20. **Pries AR, Secomb TW.** Modeling structural adaptation of microcirculation. *Microcirculation* 15: 753–764, 2008.
21. **Pries AR, Secomb TW.** Origins of heterogeneity in tissue perfusion and metabolism. *Cardiovasc Res* 81: 328–335, 2009.
22. **Pries AR, Secomb TW, Gaehtgens P.** Biophysical aspects of blood flow in the microvasculature. *Cardiovasc Res* 32: 654–667, 1996.
23. **Qian X, Brennan MP, Dione DP, Dobrucki WL, Jackowski MP, Breuer CK, Sinusas AJ, Papademetris X.** A non-parametric vessel detection method for complex vascular structures. *Med Image Anal* 13: 49–61, 2009.
24. **Schreiner W, Neumann F, Neumann M, Karch R, End A, Roedler SM.** Limited bifurcation asymmetry in coronary arterial tree models generated by constrained constructive optimization. *J Gen Physiol* 109: 129–140, 1997.
25. **Steinman DA, Taylor CA.** Flow imaging and computing: large artery hemodynamics. *Ann Biomed Eng* 33: 1704–1709, 2005.
26. **Stosic T, Stosic BD.** Multifractal analysis of human retinal vessels. *IEEE Trans Med Imaging* 25: 1101–1107, 2006.
27. **Tawhai MH, Burrowes KS.** Modelling pulmonary blood flow. *Respir Physiol Neurobiol* 163: 150–157, 2008.
28. **Walls JR, Coultas L, Rossant J, Henkelman RM.** Three-dimensional analysis of vascular development in the mouse embryo. *PLoS ONE* 3: e2853, 2008.
29. **West GB, Brown JH, Enquist BJ.** The fourth dimension of life: fractal geometry and allometric scaling of organisms. *Science* 284: 1677–1679, 1999.
30. **Zhou YF, Kassab GS, Molloi S.** In vivo validation of the design rules of the coronary arteries and their application in the assessment of diffuse disease. *Phys Med Biol* 47: 977–993, 2002.